Journal of Fluids and Structures 22 (2006) 557–575

JOURNAL OF
FLUIDS AND
STRUCTURES

www.elsevier.com/locate/jfs

Modal analysis of measurements from a large-scale VIV model test of a riser in linearly sheared flow

H. Lie*, K.E. Kaasen

MARINTEK, P.O.Box 4125 Valentinlyst, N-7450 Trondheim, Norway

Received 27 September 2004; accepted 9 January 2006

Abstract

Large-scale model testing of a tensioned steel riser in well-defined sheared current was performed at Hanøytangen outside Bergen, Norway in 1997. The length of the model was 90 m and the diameter was 3 cm. The aim of the present work is to look into this information and try to improve the understanding of vortex-induced vibrations (VIV) for cases with very high order of responding modes, and in particular to study if and under which circumstances the riser motions would be single-mode or multi-mode. The measurement system consisted of 29 biaxial gauges for bending moment. The signals are processed to yield curvature and displacement and further to identify modes of vibration. A modal approach is used successfully employing a combination of signal filtering and least-squares fitting of precalculated mode-shapes. As a part of the modal analysis, it is demonstrated that the equally spaced instrumentation limited the maximum mode number to be extracted to be equal to the number of instrumentation locations. This imposed a constraint on the analysis of in-line (IL) vibration, which occurs at higher frequencies and involves higher modes than cross-flow (CF). The analysis has shown that in general the riser response was irregular (i.e. broad-banded) and that the degree of irregularity increases with the flow speed. In some tests distinct spectral peaks could be seen, corresponding to a dominating mode. No occurrences of single-mode (lock-in) were seen. The IL response is more broad-banded than the CF response and contains higher frequencies. The average value of the displacement r.m.s over the length of the riser is computed to indicate the magnitude of VIV motion during one test. In the CF direction the average displacement is typically 1/4 of the diameter, almost independent of the flow speed. For the IL direction the values are in the range 0.05–0.08 of the diameter. The peak frequency taken from the spectra of the CF displacement at riser midpoint show approximately to be equal to the Strouhal frequency. The peak frequency in IL direction was typically twice the Strouhal frequency.

Keywords: Riser; Vortex; Vibration; Experiment; Modal; Aliasing

1. Introduction

Slender marine structures such as marine cables, pipelines and risers may be set in oscillation by a constant current. The excitation is caused by vortices that are shed alternatingly from either side of the structure hence the name vortex-induced vibration (VIV). For marine structures VIV is important with respect to fatigue damage. Also VIV may cause

---

*Corresponding author. Tel.: +47 7359 5828; fax: +47 7351 0034.
E-mail address: Halvor.Lie@marintek.sintef.no (H. Lie).

0889-9746/$ - see front matter © 2006 Elsevier Ltd. All rights reserved.
doi:10.1016/j.jfluidstructs.2006.01.002

an increase in the current drag on the riser. For design of marine cables and risers it is therefore important to have models that can predict VIV with realism.

The phenomenon of VIV is described extensively in the literature; see for instance Blevins (1990) and Vandiver (1993). For a fixed, rigid circular cylinder in a uniform flow directed normally to its axis the vortex-shedding frequency is

$$f_s = \mathrm{St}\,\frac{U}{D}, \tag{1}$$

where U is the free-stream speed and D is the cylinder diameter. The Strouhal number, St, is a function of the Reynolds number (Sheppard and Omar, 1992). In the subcritical range ($300 < \mathrm{Re} < 1.5 \times 10^5$) St varies little and has a value around 0.2. The oscillating force will mainly be directed normally to the flow, hence the terms cross-flow (CF) force and CF vibration. A smaller force component will act in the direction of the current. The frequency of this in-line (IL) force is twice that of the CF force.

When the cylinder is free to move in the transverse direction, yet with resistance from springs, it will respond to the cyclic load from the vortex shedding. The magnitude of the motion depends on the force of the vortex shedding and the responsiveness of the cylinder, as determined by its mass, added mass, damping coefficients and the stiffness of the springs. If the natural resonant frequency of the cylinder is not too far from the Strouhal frequency *lock-in* or *synchronization* may happen. In this case vortices are shed at the actual frequency of oscillation and not at the rate predicted by Eq. (1). In other words, it is the motion of the cylinder that controls the vortex shedding. The frequency of oscillation may not be exactly equal to the expected resonant frequency of the cylinder either. This is because the process of forming and shedding vortices alters the cylinder's added mass. The added mass will be different from the still water value, causing the resonant frequency to shift somewhat too. The change in added mass can be negative or positive, causing the natural frequency to go up or down. This is demonstrated in experiments by Sarpkaya (1978) and Gopalkrishnan (1993), who found that both added mass and damping depend on frequency and amplitude. See also Vikestad (1998). The damping will increase with increasing amplitudes of oscillation and will cause the VIV amplitude to be moderate, even in the case of lock-in, when it gets to be equal to about one cylinder diameter.

For taut cables and risers a multitude of natural frequencies of response exists (Lie et al., 1998). In the non-lock-in case the vortex-induced oscillations will be irregular, consisting of the natural frequencies of the structure plus the frequencies of the vortex-shedding taking place along the length of the structure. Waves will travel up and down the structure. Since such structures have many modes of response and many natural frequencies, there are many possibilities for lock-in. When lock-in happens the response will in general be unimodal and have the character of a standing wave. Which mode will respond depends on which natural frequency is closest to the Strouhal frequency. For structures of large vertical extent, the depth variation of the current can be large. Consequently, the Strouhal frequency may vary considerably over the structure's length, having the effect that several modes can be candidates for lock-in oscillation. The mechanism of frequency shifting through added-mass variation blurs the unique relationship between mode-shape and still-water eigenfrequency. This means that it is not always possible to tell which mode is in action from observations of frequency. From model tests with a taut cable in sheared flow, Lie et al. (1997) report an observation of a second-mode lock-in oscillation that suddenly changed into a third-mode lock-in while the VIV frequency remained unchanged.

Model testing has given valuable insight in the phenomenon of VIV. Based on experimental results, several empirical computer models have been constructed, such as SHEAR7 (Vandiver and Lee, 2003), VIVANA (MARINTEK, 2001), VIVA (Triantafyllou et al., 1999) and ViCoMo (Moe et al., 2001). These models, aimed at solving engineering problems, suffer from one common shortcoming, as they do not include IL response. This is partly a consequence of lack of IL data from experiments and partly underestimation of the importance of IL vibrations for fatigue damage. The alternative to empirical models is computational fluid dynamics (CFD) models, see Herfjord et al. (1999), Étienne et al. (2001) and Willden and Graham (2001). Such models are based on basic hydrodynamic theory alone, but require in general too large computational resources to be attractive as tools for solving engineering problems.

Also, full-scale field experiments have been carried out. One purpose of such tests is to see how a real riser behaves under realistic conditions, which involve high Reynolds numbers, realistic sea currents and influence by waves [cf. Kaasen et al. (2000)]. Data from field tests can also be used for verification of numerical models, but the usefulness in this respect has often been limited due to imprecise knowledge of the depth variation of the speed and direction of the current. Beside the difficulties in instrumentation and data acquisition, the main drawback with field measurements as compared to basin testing is the lack of possibility of choosing the test conditions.

2. The Hanøytangen experiment

Tests of a tensioned large-scale riser model were performed at Hanøytangen outside Bergen on the west coast of Norway in 1997; see Huse et al. (1998). One purpose of the test was to obtain high modes of CF and IL VIV in a well-defined sheared flow. The test set-up is illustrated in Fig. 1. The test site is a 180 m long floating quay at 97 m depth. The riser model was attached to a floating vessel outside the quay that was pulled by a rope system and a motor vehicle on the quay. The riser model was kept at constant tension by a buoyancy arrangement, as seen in the figure. By moving the vehicle at a constant speed, the riser was exposed to a triangular current profile. In this way a well-defined current profile was obtained. The constant speed at upper riser end was systematically varied between 0.16 and 2 m/s. The riser was furnished with transducers for measuring bending moment in two orthogonal directions every 3 m down the riser, which means that IL- and CF-induced moments were measured at 29 positions. In addition, two-directional inclinometers and tension transducers were installed at both ends. The transducers were sampled at a rate of 120 Hz.

The Hanøytangen experiments also included tests in which a second parallel riser was towed behind the first one. The purpose of these tests was to study the onset of collision between risers due to wake interaction between individual risers.

This article describes the methods used for identifying and analysing the measured data of the single riser VIV tests. In a separate article by Baarholm et al. (2006a, b) the results are taken further and studied with respect to fatigue. Huse et al. (1999) have treated the Hanøytangen experiment with respect to axial vibrations.

The Hanøytangen riser model was exposed to a linearly sheared current profile. The current speed ranges from $U_{\max}$ at the free surface to almost zero current at the lower riser end, see Fig. 1. Key data for the riser model are given in Table 1.

3. Simplified study of a tensioned riser

Some key features of riser dynamics can be illustrated by inspecting the eigenfrequencies and mode-shapes of a tensioned beam with moment-free supports at both ends. Starting with the eigenfrequencies for a tensioned string without bending stiffness and a nontensioned beam of equal length L and mass per unit length m, we have

$$f_{n,\text{string}} = n\,\frac{1}{2}\sqrt{\frac{T}{mL^2}}, \tag{2}$$

$$f_{n,\text{beam}} = n^2\,\frac{\pi}{2}\sqrt{\frac{EI}{mL^4}}; \tag{3}$$

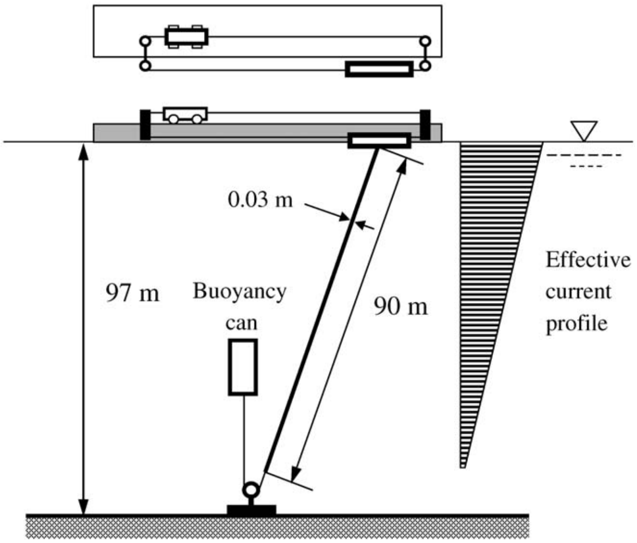

Fig. 1. Test set-up at Hanøytangen (single riser configuration).

Table 1
Key data for the Hanøytangen riser model

Length (m)	90
Outer diameter (m)	0.03
Inner diameter (m)	0.026
Modulus of elasticity (N/m^2)	2.1×10^{11}
Bending stiffness (Nm^2)	3.64×10^3
Riser density (kg/m^3)	3211
Mass (kg/m)	2.27
Mass ratio (mass/mass of displaced water)	3.13
Length/diameter ratio	3000
Tension at top (N)	3700

here, n is the mode number, T is the constant tension in the string, and I is the moment of inertia of the beam. The actual riser will not have constant tension along its length, but Eq. (2) represents a good approximation if tension variation is moderate and T is taken as the tension at the midpoint of the riser.

The tensioned string and nontensioned beam have identical mode-shapes given as sine functions for the actual boundary conditions. The mode-shape for eigenfrequency n is given by

$$\varphi_n(z) = A_0 \sin\left(\frac{n\pi}{L} z\right), \tag{4}$$

where A_0 is an unknown amplitude. This mode-shape will give identical modal mass for all modes, and also for the string and beam case. Hence, the nth eigenfrequency for the tensioned beam, $f_{n,\text{t-beam}}$ can be found by the simple relation (Timoshenko et al., 1974):

$$f_{n,\text{t-beam}} = \sqrt{f_{n,\text{string}}^2 + f_{n,\text{beam}}^2} \tag{5}$$

The tow speed that will excite an eigenfrequency can be found from Eq. (1), i.e.

$$U_n = \frac{f_{n,\text{t-beam}} D}{St}, \quad n = 1, 2, \ldots, \tag{6}$$

where D is the riser diameter. Fig. 2 shows the eigenfrequency and the tow speed as functions of n for the Hanøytangen riser model. Values for a nontensioned beam, a tensioned string and a tensioned beam are shown for $\text{St} = 0.17$. This value of the Strouhal number is lower than the usually quoted 0.2, but has been found to apply for moving cylinders. [cf. Fig. 3 in Larsen and Koushan (2005)]. As an approximation one may estimate the IL response frequency to be two times the CF response frequency. For a tensioned string this means that the IL mode number will be twice the number of the CF mode, whereas for an untensioned beam it will be lower, due to the quadratic relationship between n and frequency in Eq. (3). This is discussed more extensively by Baarholm et al. (2006b).

The eigenfrequency for the tensioned riser is seen to follow the tensioned string case for lower modes, and then become closer to the untensioned beam case. This means that the stiffness of the tensioned riser will be tension-dominated for the lower modes, while the bending stiffness becomes increasingly important with increasing mode order.

In the towing speed range 0.16–2.0 m/s one may expect that CF modes ranging from 7 to 33 will be excited. For IL, the corresponding range of modes is estimated to be 9–50.

4. Processing of measurements—modal approach

With respect to fatigue damage, riser curvature is the most important parameter as it is directly related to wall stresses. At Hanøytangen, curvature was measured almost directly by sensors for the bending moment. Due to measurement noise the measured curvature cannot be used without processing. A major purpose of such a processing is to give good estimates of the true curvature, not only at the locations of the gauges, but globally, i.e. at every point on the riser.

As VIV usually is presented, analysed and compared in terms of displacement, derivation of displacement from the curvature measurements should also be an objective of the processing.

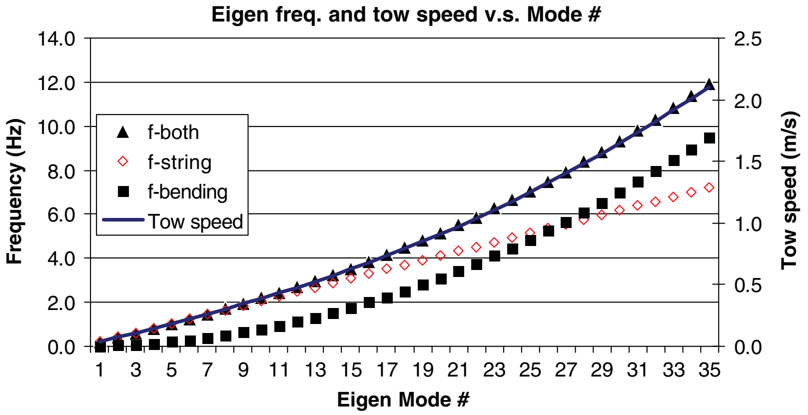

Fig. 2. Simplified estimates of CF frequencies and towing speeds as functions of mode number (calculated with zero added mass).

In order to study the nature of VIV under the prevailing experimental conditions, modal decompositioning is informative. For the processing and analysis described in the following a modal approach has therefore been chosen.

The modal analysis technique has previously been applied to combined measurements of acceleration and angular rate on a full-scale drilling riser (Kaasen et al., 2000). A similar approach has been used by Trim et al. (2005). A different modal technique, not utilizing a priori information, has been used by Kleiven (2002).

Since the Hanøytangen riser measurements are curvature, it should in principle be possible to derive displacement by double numerical integration. However, as demonstrated below, due consideration must be given to noise filtering and signal conditioning. The direct integration approach does not give information about the modal decompositioning of the response or the response between the points of measurement. To overcome these shortcomings a modal analysis approach was chosen for the processing of the Hanøytangen data, as described in the following.

Assuming that the top-tensioned riser deviates little from the vertical and that the dynamical process of riser motion is approximately linear, the time varying shape of the riser can be composed as a series of eigenfunctions or mode-shapes:

$$x(t,z)=\sum_{n=1}^{\infty} w_n(t)\varphi_n(z), \quad z\in[0,L], \tag{7}$$

where t is the time, z the vertical coordinate, L the length of the riser, $x(t,z)$ the horizontal displacement of the riser, $\varphi_n(z)$ the mode-shape, $n=1,2,3,\ldots$, and $w_n(t)$ the modal weight, $n=1,2,3,\ldots$.

The mode-shapes of riser *curvature* are derived from the displacement mode-shapes as

$$\theta_n(z)=\frac{\mathrm{d}^2\varphi_n(z)}{\mathrm{d}z^2}. \tag{8}$$

The curvature of the riser can then be expressed as the series

$$\kappa(t,z)=\sum_{n=1}^{\infty} w_n(t)\theta_n(z). \tag{9}$$

It is seen that the series for displacement (7) and curvature (9) share the modal weights, whereas the mode-shapes differ. If the mode-shapes of displacement are sinusoidal or can be approximated with sinusoids, i.e.

$$\varphi_n(z)=\sin\frac{n\pi}{L}z, \tag{10}$$

the mode-shapes of curvature become sinusoidal too and Eq. (9) can be written

$$\kappa(t,z)=\sum_{n=1}^{\infty} w_n(t)\theta_n(z)\approx-\sum_{n=1}^{\infty} w_n(t)\left(\frac{n\pi}{L}\right)^2\varphi_n(z)=\sum_{n=1}^{\infty} v_n(t)\varphi_n(z). \tag{11}$$

In other words, the modal weight factors for displacement and curvature with respect to $\varphi_n(z)$ are related as

$$v_n(t)=-\left(\frac{n\pi}{L}\right)^2 w_n(t). \tag{12}$$

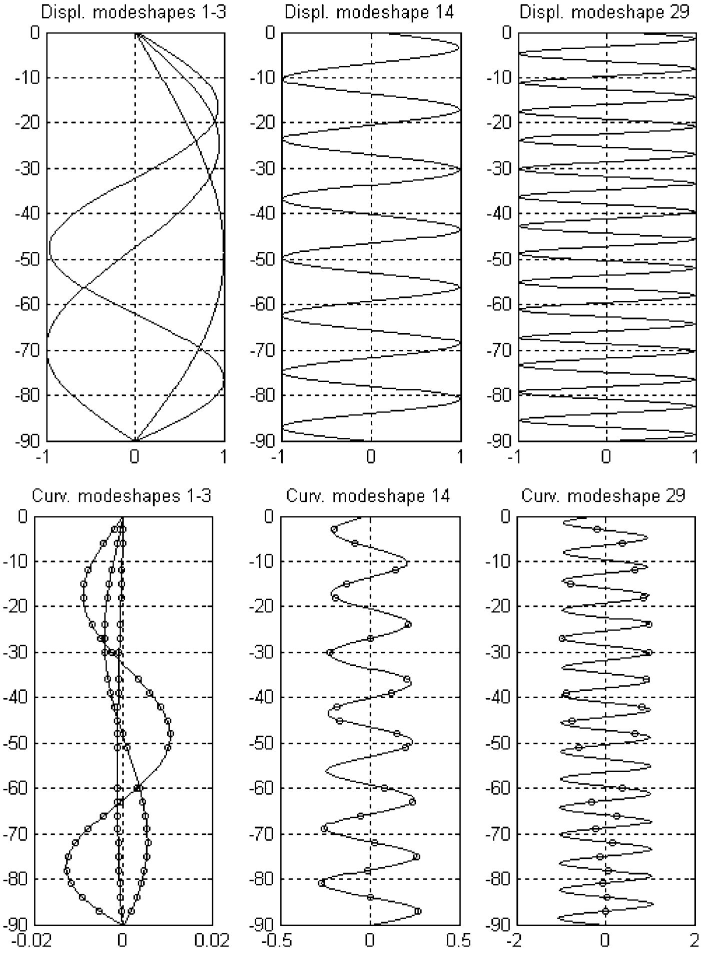

Fig. 3. Example of mode-shapes of displacement (top) and curvature. Circles indicate locations of sensors (note differences in horizontal scaling for curvature mode-shapes).

Curvature is measured at a number of positions on the riser, z_m, $m = 1, \ldots, M$:

$$c_m(t) = \kappa(t, z_m) + \eta_m(t), \quad m = 1, \ldots, M; \tag{13}$$

here, $c_m(t)$ is the measurement signal. It is equal to true curvature plus measurement noise, η_m. (strictly, it is the bending moment that was measured, but as curvature and bending moment differ only by a factor, the term "measurement" is used for both.)

The task is to calculate the time- and position-dependent riser displacement $x(t, z)$ from the M discrete curvature measurements, It is assumed that the mode-shapes θ are known. Further, it is assumed that it is sufficient to use N terms in series (7) and (9) to describe the curvature:

$$c_m(t) = \sum_{n=1}^{N} w_n(t)\theta_n(z_m) + \eta_m(t), \quad m = 1, 2, \ldots, M. \tag{14}$$

This equation can be expressed in vector notation: first, form the vectors of mode-shape curvatures evaluated at the points of measurement

$$\boldsymbol{\theta}_n = [\theta_n(z_1), \theta_n(z_2), \ldots, \theta_n(z_M)]^{\mathrm{T}}, \quad n = 1, 2, \ldots, N; \tag{15}$$

then form the $M \times N$ matrix

$$\boldsymbol{\Theta} = [\boldsymbol{\theta}_1, \boldsymbol{\theta}_2, \ldots, \boldsymbol{\theta}_N] \tag{16}$$

and the vectors of curvature measurements, measurement noise and modal weights

$$\boldsymbol{c}(t) = [c_1(t), c_2(t), \ldots, c_M(t)]^{\mathrm{T}}, \tag{17}$$

$$\boldsymbol{\eta}(t) = [\eta_1(t), \eta_2(t), \ldots, \eta_M(t)]^{\mathrm{T}}, \tag{18}$$

$$\boldsymbol{w}(t) = [w_1(t), w_2(t), \ldots, w_N(t)]^{\mathrm{T}}. \tag{19}$$

Eq. (14) can now be written as

$$\boldsymbol{c}(t) = \boldsymbol{\Theta}\boldsymbol{w}(t) + \boldsymbol{\eta}(t). \tag{20}$$

If the number of unknown modal weights equals the number of measurements ($N = M$), the modal weights can be found (neglecting the measurement noise, which is unknown):

$$\hat{\boldsymbol{w}}(t) = \boldsymbol{\Theta}^{-1}\boldsymbol{c}(t). \tag{21}$$

We see that for each time instant the modal weights are obtained from the curvature measurements by a constant, linear mapping and vice versa. The solution for the modal weights is marked with a circumflex to show that, due to the existence of measurement noise, it will deviate more or less from the true solution. The time-varying displacement and curvature for the entire riser (i.e. not only the points of measurement) are found by substituting the M components of the solution vector in Eq. (21) into (7) and (9), respectively.

If it can be argued that fewer than M mode-shapes participate significantly in the riser motion, the system of Eq. (20) can be solved in the least-squares sense. In this case ($N<M$) the estimate of modal weights becomes

$$\hat{\boldsymbol{w}}(t) = (\boldsymbol{\Theta}^{\mathrm{T}}\boldsymbol{\Theta})^{-1}\boldsymbol{\Theta}^{\mathrm{T}}\boldsymbol{c}(t) = \boldsymbol{H}\boldsymbol{c}(t). \tag{22}$$

This expression reduces to the previous form (21) (i.e. $\boldsymbol{H} = \boldsymbol{\Theta}^{-1}$) when the number of mode-shapes is M, i.e. when the matrix $\boldsymbol{\Theta}$ becomes square. Hence, Eq. (22) can be regarded as the general form of the estimator and Eq. (21) a special case.

Estimator (22) can be applied to CF and IL motions separately, yet with the matrix $\boldsymbol{H}$ constructed differently (depending on how many and which mode-shapes to use). During installation of the riser at Hanøytangen, some of the 29 sensors for bending moment (~curvature) failed. For the CF motion 24 sensors remained usable. For the IL motion the number was 26. This means that the maximum number of identifiable modal weights (i.e. N) is 24 for CF and 26 for IL. Using fewer modes than the maximum number will in general reduce estimation errors.

To use this method for estimation of the modal weights, mode-shapes of displacement and curvature were calculated with the finite elements computer program RIFLEX (MARINTEK, 2003). The calculation was done for a numerical model with no damping and a hydrodynamic-added mass coefficient of 1.0. Fig. 3 shows examples of the mode-shapes. The displacement mode-shapes are normalized to unity with respect to the maximum norm. It is seen that the amplitudes of the corresponding mode-shapes of curvature increase strongly with mode number. The mode-shapes resemble sinusoids, but the wavelength decreases somewhat towards the bottom. This is a consequence of the gradually decreasing tension towards the bottom. A corresponding increase in amplitude is seen, but the effect is not prominent.

The FEM-based mode-shapes were used in the analysis of the Hanøytangen data. However, tests with sinusoidal mode-shapes gave nearly identical results. One should bear in mind that in reality true eigenmodes do not exist for a structure such as the Hanøytangen riser. The reason for this is the existence of various nonlinearities and time-variances:

(i) time-varying tension;
(ii) sag due to current drag and displacement of upper riser end during tests;
(iii) nonlinear damping;
(iv) temporal and spatial variations in added mass and damping as functions of frequency and amplitude of vibration.

Together these factors may cause the actual riser dynamics to deviate significantly from the idealized linear model used in the calculation of the eigenmodes. This does not destroy the usability of estimator (22). The reason for this is that it is not really necessary that the functions θ_n in Eq. (9) be eigenfunctions. What is important is that the set of functions are linearly independent and complete in the sense that series (9) can describe any curvature variation with z.

5. Error and identifiably analysis

Fig. 3 indicates that the amplitudes of the curvature mode-shapes increase strongly with the mode number. Essentially the amplitude is proportional to the mode number squared. This means that detecting a low mode of riser vibration may be difficult since the corresponding curvature will be small. An example illustrates this. In Hanøytangen test number 39 the riser was towed at a speed of 0.64 m/s. The maximum Strouhal frequency (i.e. the one corresponding to the speed of the riser's top) is around 4.3 Hz. The peaks of the curvature spectra were found to lie in the range 2–4 Hz. According to Fig. 2 this range of Strouhal frequencies corresponds approximately to the natural frequencies of modes 10–17. The estimation method described above was applied to the data, using mode-shapes 1–24 in the matrix $\boldsymbol{\Theta}$. With anticipated modes 10–17 occurring in the response, one would expect that the low-numbered modes be estimated at approximately zero. However, as shown in Fig. 4, the first mode totally dominates the response. Considering the observed range of response frequencies, this is physically impossible. The conclusion that can be drawn from this is that the level of noise on the curvature measurements may prevent identification of modes. The influence of the noise is studied further in the following.

According to Eqs. (20) and (22) the estimation error of the modal weights is

$$\boldsymbol{e}(t) = \boldsymbol{H}\boldsymbol{\eta}(t). \tag{23}$$

Here $\boldsymbol{\eta}(t)$ is the vector of measurement noise on the curvature. Assuming the components of $\boldsymbol{\eta}(t)$ to be uncorrelated with equal variance ${\sigma_\eta}^2$ the covariance matrix $\boldsymbol{E}$ of the estimation error becomes

$$\Sigma = E\{\boldsymbol{e}\boldsymbol{e}^{\mathrm{T}}\} = \boldsymbol{H}E\{\boldsymbol{\eta}\boldsymbol{\eta}^{\mathrm{T}}\}\boldsymbol{H}^{\mathrm{T}} = \boldsymbol{H}\boldsymbol{H}^{\mathrm{T}}\sigma_\eta^2 = (\boldsymbol{\Theta}^{\mathrm{T}}\boldsymbol{\Theta})^{-1}\sigma_\eta^2; \tag{24}$$

here, $E\{\}$ denotes statistical expectation. The diagonal of the matrix Σ contains the variances of the estimation errors of the modal weight factors:

$$[\sigma_{e_1}^2, \sigma_{e_2}^2, \sigma_{e_3}^2, \ldots] = \mathrm{diag}(\Sigma). \tag{25}$$

The standard deviations, σ_{e_i}, $i = 1, 2, \ldots$, are shown in Fig. 5 using unit variance of curvature error noise ($\sigma_\eta^2 = 1$) as input. Note the log scale on the vertical axis. One can see that the low modes are very sensitive to measurement noise. (For regularly placed sensors and sinusoidal mode-shapes the points in the figure would decay as $1/n^2$. The deviation from this trend is an effect of missing sensors.)

According to the instrumentation report the overall accuracy of the bending moment transducers is expected to be better than about 2–3 percent of typical signal level. For a bending moment M the strain in the outer wall of the riser is

$$\varepsilon = \frac{Mr}{EI}, \tag{26}$$

where r is the outer radius and EI the bending stiffness, cf. Table 1. For a typical value of 15 N m for M and assuming 2.5% error, we get for the error in measured strain:

$$\sigma_\varepsilon = 0.025\varepsilon = 0.025\,\frac{15 \times 0.015}{3.64 \times 10^3} \approx 1.5 \times 10^{-6}. \tag{27}$$

Since, as argued above, Test 39 cannot include low-numbered modes, virtually the entire estimated first modal weight $\hat{w}_1(t)$ must be error due to measurement noise, i.e.

$$E\{\hat{w}_1(t)^2\} = \sigma_{e_1}^2. \tag{28}$$

Based on this assumption Eq. (24) enables us to estimate the standard deviation of measurement noise (in terms of units of curvature). Let a be element 1,1 of the matrix $(\boldsymbol{\Theta}^{\mathrm{T}}\boldsymbol{\Theta})^{-1}$ in Eq. (24). Then we have

$$\sigma_{e_1}^2 = a\sigma_\eta^2. \tag{29}$$

Knowing a and getting σ_{e_1} from Eq. (28) we obtain the measurement noise σ_η from Eq. (29).

For Test 39, the above procedure gives $\sigma_\eta = 1.7 \times 10^{-4}\,\mathrm{m}^{-1}$. The corresponding strain in the riser wall is $\sigma_\varepsilon = r\sigma_\eta = 2.6 \times 10^{-6}$, i.e. 2.6 micro-strains, which is in fair agreement with Eq. (27). It must be remembered that the noise figure must be expected to contain some contributions from various other noise sources than those related to pure transducer error, e.g. high-mode aliases (see below).

Having in this way an estimate of the error of the curvature measurement, σ_η, is very useful because based on it the absolute level of the estimation errors (25) can be assessed. The criterion for accepting an estimate, $\hat{w}_n$, for a modal weight must be that the r.m.s. value of the modal weight significantly exceed the corresponding noise level, σ_{e_n}.

There are two options for the way estimator (22) for modal weights can be used

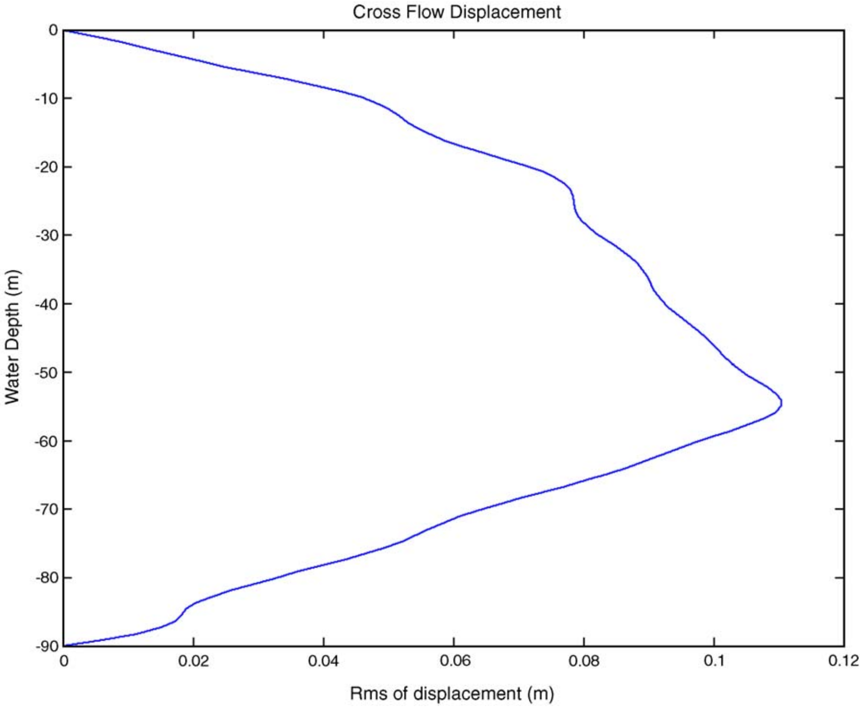

Fig. 4. Standard deviation of cross-flow displacement along the riser, constructed from 24 given mode-shapes and estimated corresponding modal weights. Hanøytangen test no. 39.

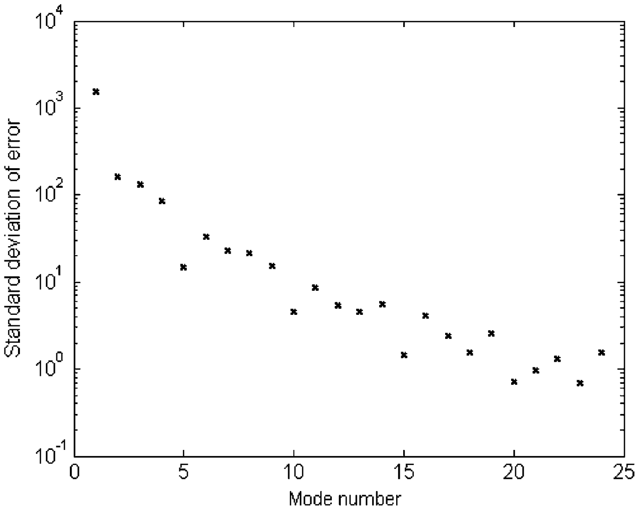

Fig. 5. Error of estimates of modal weights assuming uncorrelated noise of unit variance on all measurements.

1. Estimation is carried out with the maximum number of mode-shapes present, i.e. 24 for CF and 26 for IL. Modal weights that fall below the noise level or are not physical with regard to frequency content are discarded. A criterion for the latter case is that the responding frequencies lie far below or far above reasonable Strouhal frequencies.
2. Estimation is carried out only for the modes that are likely to be present according to prior judgement based on current speed and spectral analysis of the measurements. For example, if it is found that modes 11–20 are likely to participate, only mode-shapes 11–20 enter in matrix $\boldsymbol{\Theta}$.

Option 2 was preferred for two reasons. (i) If the mode-shapes had been orthogonal the two options would be equivalent. The mode-shapes used in this work are nearly orthogonal when viewed as continuous functions of z. However, when considered only at the points of measurement, i.e. as discrete functions of z, the mode-shapes are not orthogonal. Lack of orthogonality means that the mode-shapes can partly act as substitutes for one another. Discarding mode-shapes—like in option 1 above—means throwing away information the remaining, accepted mode-shapes could make use of. (ii) The second option involves fewer modes and consequently quicker computation.

6. Spatial aliasing

As pointed out above, the maximum number of modes that can be determined from the measurements is equal to the number of measurements. Does this mean that any modes can be determined as long as their number does not exceed the number of measurements? For example, is it possible to calculate modes 20–40 for the Hanøytangen case? The answer is (to the authors' knowledge) no, owing to *aliasing*. This phenomenon, well known from signal sampling, is best explained by assuming that the mode-shapes are purely sinusoidal. Consider the 29th and the 31st mode-shape. As shown in Fig. 6, the samples of these two mode-shapes are identical (except for sign). It is impossible to distinguish the modes from one another by observing their samples; mode-shape 29 is an alias for mode-shape 31 and vice versa. Likewise, mode-shapes 28 and 32 are aliases, and so on. The 30th mode-shape (the "Nyquist mode") escapes detection as it is sampled at its nodes.

One might think that it should be possible to distinguish modes that are (partly) geometrically aliased by looking at their frequency content. However, due to the uncertainty about the dynamic properties of the VIV model, it is in practice not possible to discriminate neighbouring mode-shapes on the basis of frequency. As a consequence of this, only modes up to and including the 29th were used in the analysis.

To remove signal components that frequency-wise are thought not to belong to the set of mode-shapes chosen in the analysis (cf. calculation option 1 above) band-pass filtering was applied to the measurements before using estimator (22). The filtering was applied in the frequency domain by simply discarding unwanted frequency components. An example of band-pass filtering is shown in Fig. 7. It can be seen that in addition to smoothing the signal the filter has removed the signal's mean value and slowly varying components.

7. Example of results

Thirteen tests from the Hanøytangen data were selected for VIV analysis using the methods described above. In the following, the results for one of the tests (Test 38) are presented in detail. The length of the measured time-histories of curvature from this test is 36 s or about 100 cycles of CF vibration. The towing speed was 0.54 m/s. For CF the results are compared to a case of higher towing speed (Test 51). Following is a summary for all the 13 cases.

For each test case the results of the analysis were presented as a number of plots. CF and IL were given identical presentations. For Test 38 Fig. 8 shows the main presentation sheet for CF. The figure consists of six subfigures, (a)–(f). Fig. 8(a) shows the r.m.s values of the modal weight factors of curvature, cf. Eq. (12) (assuming sinusoidal mode-shapes). After some experimenting, modes 8–20 were selected to participate in the analysis. It is seen that modes 11–14 dominate the curvature.

Fig. 8(b) shows the r.m.s. values of the CF displacement along the riser. An interference pattern, i.e. the sum of incident and reflected waves, is clearly seen, indicating presence of the 11th mode. The small size of the ripples indicates that the response mainly consists of travelling waves (for a pure standing wave pattern one would expect the notches to extend down to zero). On the whole, the CF response is fairly constant over the riser's length. This means that either (i) the riser is excited over its entire length or (ii) the excitation takes place in the upper region, but downward travelling waves are damped little.

Fig. 8(c) shows the r.m.s. values of the participating modal weight factors of displacement. The 11th mode is dominating, which is in agreement with the wave pattern in the previous plot. The plot also shows the noise threshold, as estimated from Eq. (24) assuming a noise of $\sigma_\varepsilon = 1.5 \times 10^{-6}$ on the measured strains. The plot demonstrates that modal weight estimates are well above the noise threshold. The subfigure seems to indicate that including modes below the eighth would improve the model. This, however, was found not to be the case.

Fig. 8(d) shows the effect of the band-pass filtering, in terms of r.m.s. of curvature measurements before (crosses) and after (circles) filtering. It appears that in particular the sensor at location −42 m had been noisy. The asterisks show the r.m.s. of the residual curvature, which is the difference between the filtered curvature measurements (circles) and the

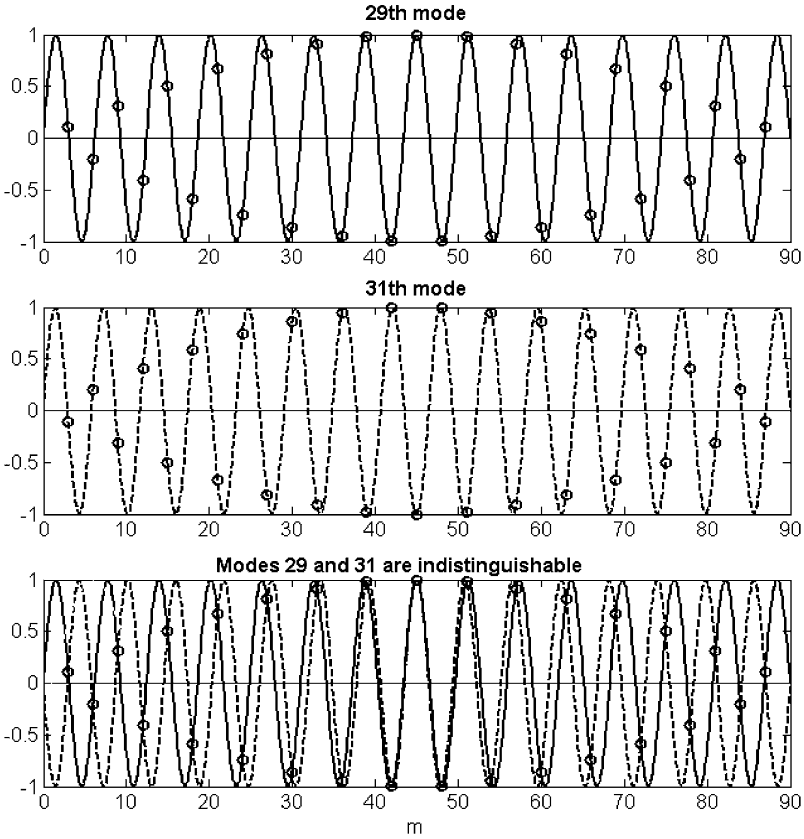

Fig. 6. Example of aliasing; 29th and 31st modes are identical at sampling points (except for sign).

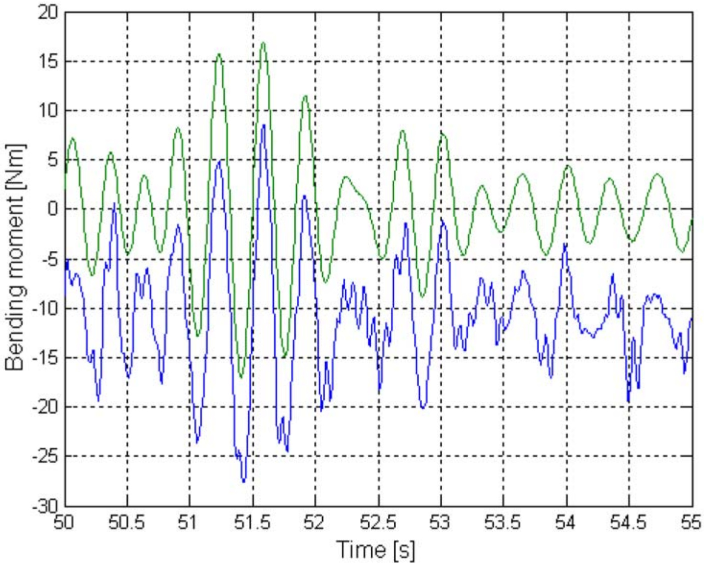

Fig. 7. Bending moment signal from cross-flow transducer no. 1 before and after band-pass filtering.

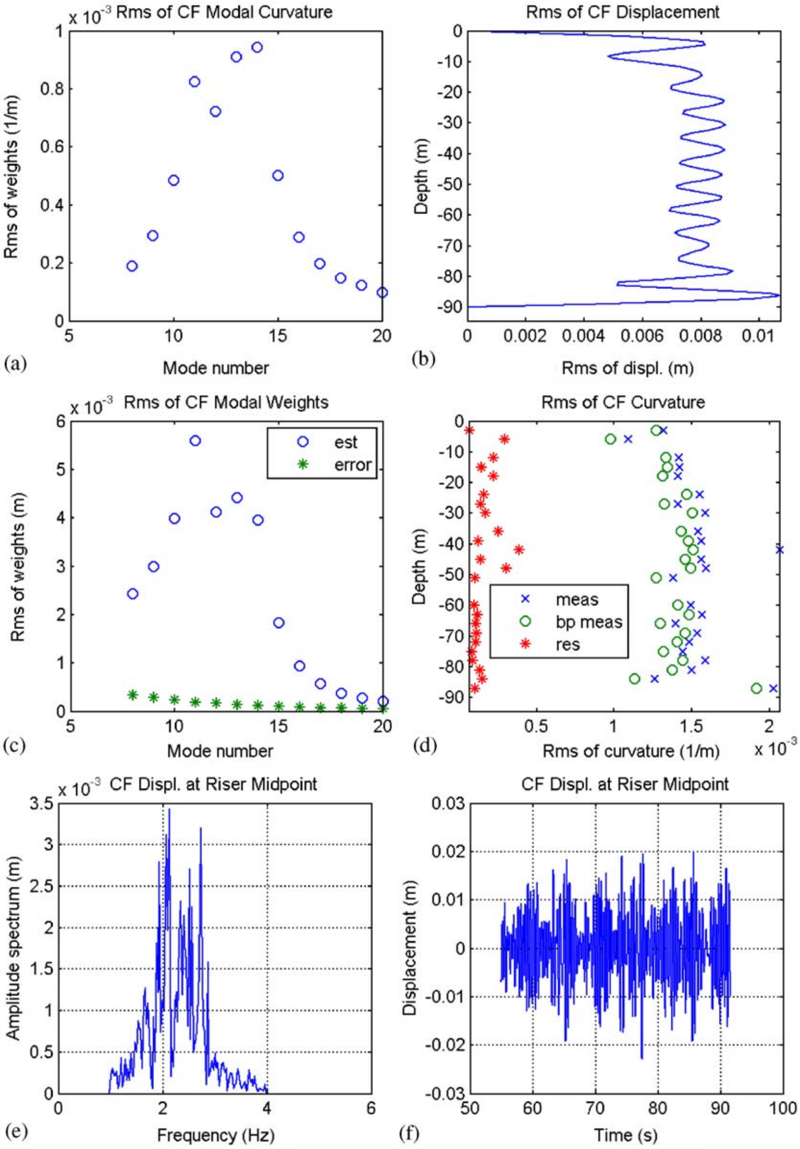

Fig. 8. Example of modal analysis. CF results for Test 38 (towing speed 0.54 m/s).

curvatures according to the fitted model, i.e. $\eta_m(t)$ in Eq. (14). The residual curvature shows how much of the signal has not been ‘‘picked up’’ in the modal analysis or ‘‘explained’’ by the model.

Fig. 8(e) shows the amplitude spectrum of the CF displacement at the middle point of the riser. ‘‘Amplitude spectrum’’ as distinct from power spectral density, simply is the Fourier amplitudes of the signal. The bulk of the CF response is seen to exist between roughly 2 and 3 Hz, the highest peaks occurring at about 2.1 and 2.7 Hz. The bounds of the band-pass filter are seen to be 1 and 4 Hz. The richness in frequency content indicates an irregular character of the response, which is corroborated by the time history in Fig. 8(f).

Fig. 9 shows a similar presentation of IL motion. The IL response is much more irregular than the CF response, as can be seen from the width of the spectrum and the high number of significantly participating modes (10–29). The bounds of the band-pass filter were 1.5 and 10 Hz, the upper frequency corresponding to about the natural frequency associated with the 31st–32nd mode, according to Fig. 2 (for an added mass higher than zero the corresponding mode number will be higher). The amplitude spectrum shows peaks at 4.2 and 5.4 Hz, i.e. twice the frequency of the peaks of the CF response in Fig. 8. There is also a peak at 8.5 Hz. Whether there is a corresponding CF component at half the

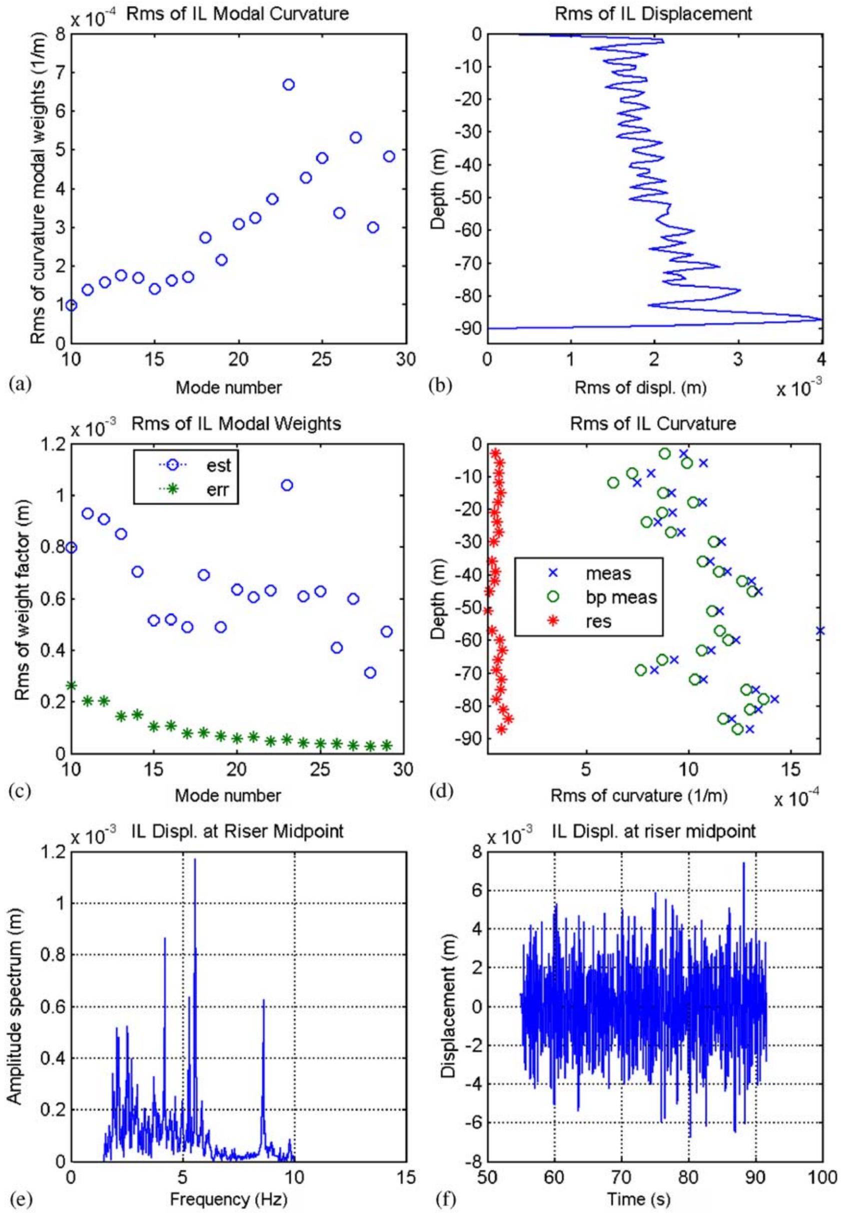

Fig. 9. Example of modal analysis. IL results for Test 38. Towing speed 0.54 m/s. Modes 10–29.

frequency is not known, as it would fall above the upper frequency (4 Hz) of the filter applied to the CF measurements. The dominant mode is number 23, which probably can be associated with the peak at 5.4 Hz. As comparison the approximate relationship in Fig. 2 ascribes a frequency of about 6 Hz to mode 23.

The highest mode number used in the analysis for IL was 29. From Fig. 9 it is seen that higher modes could have been included (as well as lower). However, aliasing prevents this, as demonstrated by Fig. 6. It is possible that the estimate of the weight factor for mode 29 (in particular) includes some aliased energy from modes above the 30th. While an upper mode of 29 is tolerable for Test 38, it is a serious problem for tests with higher towing speeds.

Fig. 10 shows results for CF for a higher towing speed, 1.14 m/s (Test 51). Comparing with Fig. 8 it is seen that more modes and higher modes participate in the response. The motion spectrum is more broad-banded. The displacement r.m.s. is seen to decline towards the bottom. This indicates that vibrations are excited at the upper part of the riser and

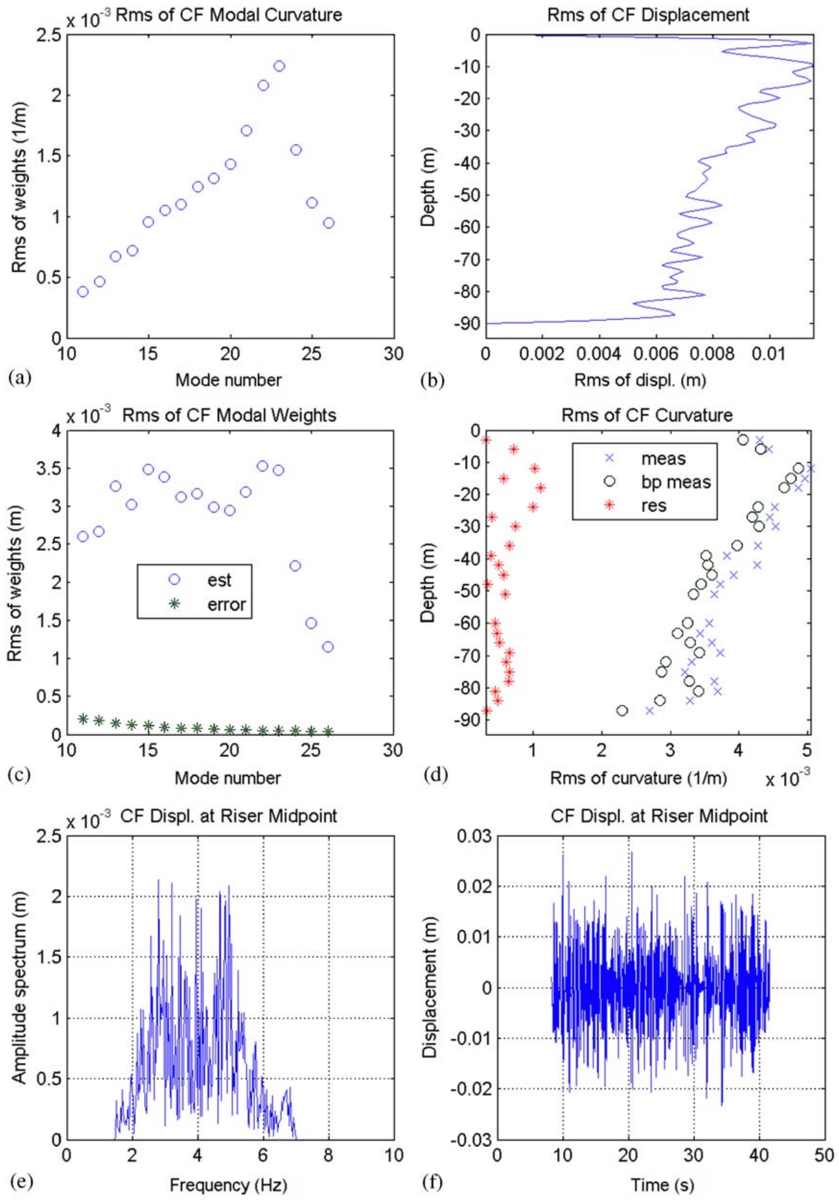

Fig. 10. Example of modal analysis. CF results for Test 51. Towing speed 1.14 m/s.

get damped as they travel downwards. This is reasonable, since higher modes imply higher horizontal speeds and in turn higher damping.

8. Example of effect of aliasing

To demonstrate the effect of aliasing estimation of modal weights for IL was repeated with mode-shapes 31–50, i.e. the aliases for mode-shapes 10–29 (in reverse order). Fig. 11 shows the results. It is seen that the modal curvatures (Fig. 11(a)) are exact mirror images of those shown in Fig. 9. Further, Figs. 9(d) and 11(d) are identical. Thus, viewed through the measurements, the two models are indistinguishable. Of course, the mode-shapes being different, the estimated displacement will differ as seen in from remainder of the plots.

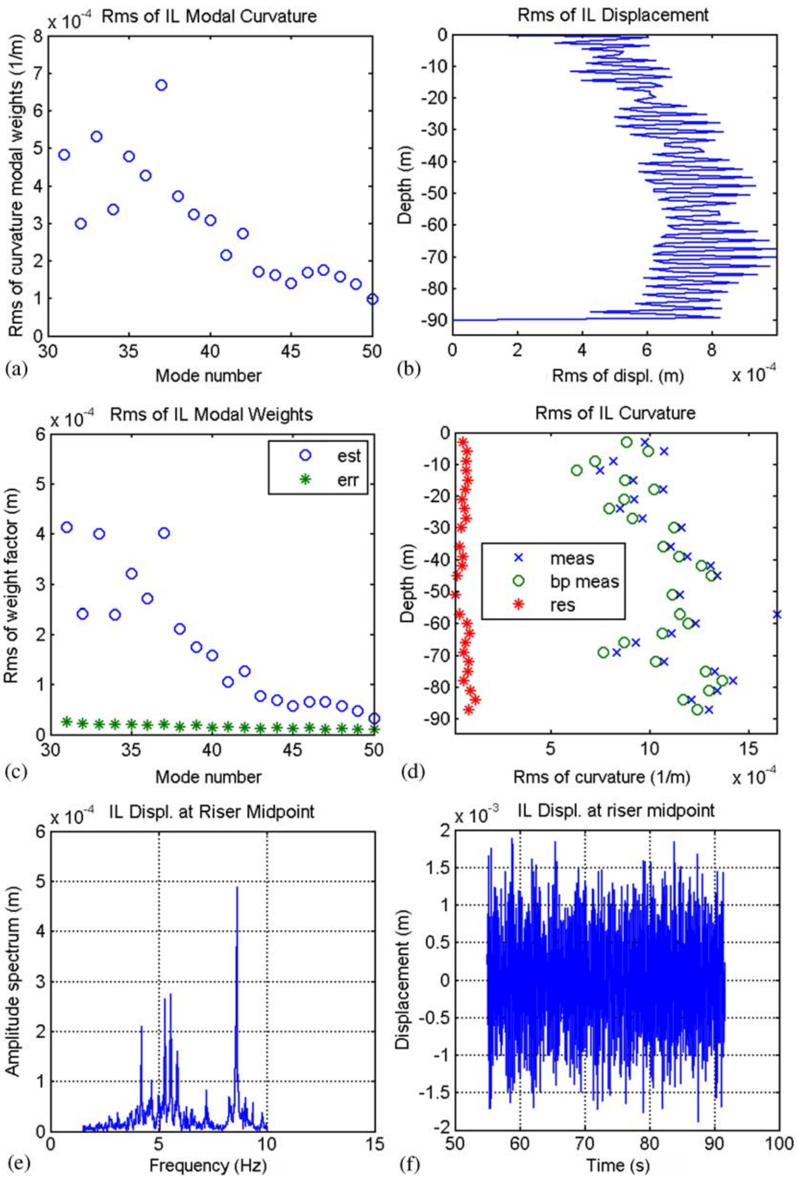

Fig. 11. Demonstration of aliasing (Test 38, IL). Processing is identical to that for Fig. 9, except that "mirror modes" 31–50 are used instead of original modes 10–29.

In this example of aliasing, sinusoidal mode-shapes were used. Considering the FEM-calculated mode-shapes (Fig. 3), aliasing as described above does not exactly apply, i.e. the samples of 29th and 31st mode-shape will not be identical. Still, the samples will be strongly correlated. Including mode-shapes above the 30th in the estimator is therefore expected to lead to very inaccurate estimates for the modal weights. Unlike the sinusoidal case, the FEM-based 30th mode-shape *is* observable through the samples, but as it is correlated with the 29th mode by 90%, using both mode-shapes will be useless.

It is possible that the problem of aliasing can be avoided or lessened if the sensors are mounted nonequidistantly. Formulating a functional for mode identifiability, it is in principle possible to maximise the identifiability with respect to sensor locations. Kaasen (2001) did this for a sensor system consisting of six accelerometers. For a system consisting of around 30 sensors the method used may not be feasible, due to the large amount of computation required.

9. Summary for the 13 analysed cases

Some key parameters and relationships based on the 13 analysed cases are presented as functions of the towing speed, which was varied from 0.16 to 1.14 m/s. Cases of higher tow speeds were excluded because of aliasing problems.

One measure of the magnitude of the VIV is the average r.m.s. taken over the length of the riser. Fig. 12 presents this for CF and IL responses. One can observe that the average r.m.s. CF displacement is about 0.25 of the diameter, and increases only a little with the towing speed. The magnitude of the displacement appears to be smaller than what is reported from similar experiments, cf. Lie et al. (1997, 1998) and Trim et al. (2005). The reason is not known. For IL, the response varies between 0.05 and 0.08 of the diameter.

Fig. 13 shows how the peak frequency of CF and IL VIV varies with the tow speed. “Peak frequency” here means the frequency of the highest spectral peak, taken from the spectra of displacement at the riser midpoint. As expected there is a clear increasing trend. The lower straight line is the Strouhal frequency (1), based on the towing speed and a Strouhal number of 0.17. The IL peak frequencies include two outliers, which is understandable considering the irregular and multi-peaked character of IL response. The upper continuous straight line represents two times the Strouhal frequency. The two straight lines would fit the data better if a lower and more representative speed than the tow speed had been shown in the figure.

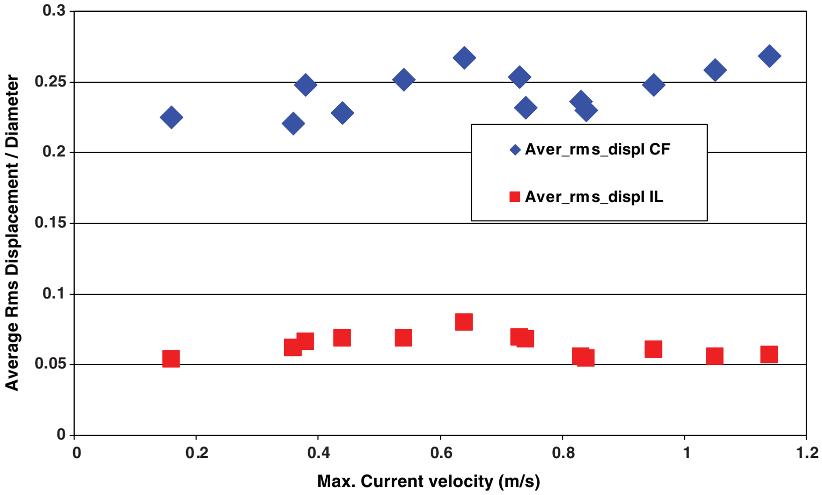

Fig. 12. R.m.s. of displacement versus flow speed at top of riser.

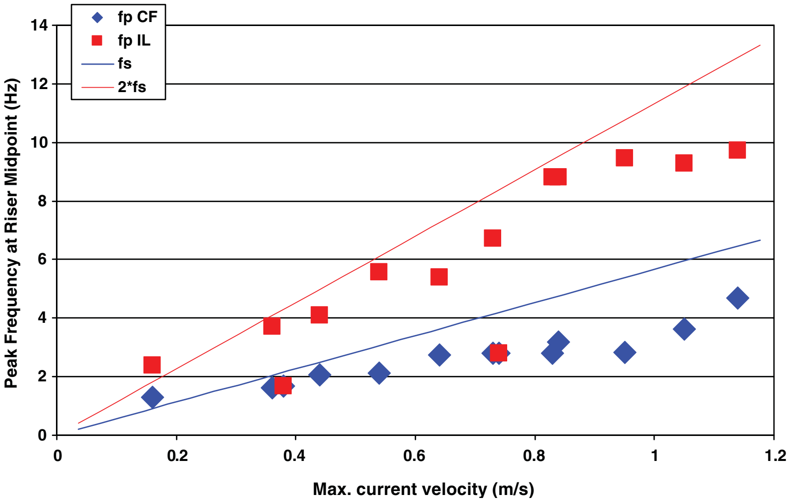

Fig. 13. Peak frequency versus flow speed at top of riser, $f_s = \mathrm{St}U/D$, where $\mathrm{St} = 0.17$.

Fig. 14 shows average curvature r.m.s., defined analogously to average displacement. For both CF and IL the average curvature increases approximately linearly or slightly progressively with towing speed, as distinct from displacement, which stayed almost constant. One observes that the IL curvature is not much smaller than CF curvature. This is an important observation, because it indicates that the IL fatigue will be in the same order of magnitude as the CF fatigue.

From the modal analysis the modal weight standard deviations, σ_{w_n} are computed. The value of n with the largest σ_{w_n} is called the largest mode with respect to displacement. Fig. 15 presents the number of the largest mode with respect to displacement for both CF- and IL-direction versus the towing speed. The results for IL response for speeds larger than 0.8 m/s are not included here, because these results are considered to be significantly hampered by the limitation on the participating modes due to aliasing. It appears from the figure that the number of the largest mode increases about linearly with the towing speed, although for CF the line does not seem to pass through the origin. Around 0.8 m/s, the IL largest mode numbers is about two times the CF largest mode number.

Kurtosis is (along with other parameters) frequently used for characterization of the probability density function of random signals. It is defined as m_4/m_2^2, where m_4 and m_2 are the fourth and second moments of the signal's distribution. For a Gaussian signal the kurtosis is 3.0, while a sinusoidal signal has a kurtosis of 1.5. Lock-in oscillation is expected

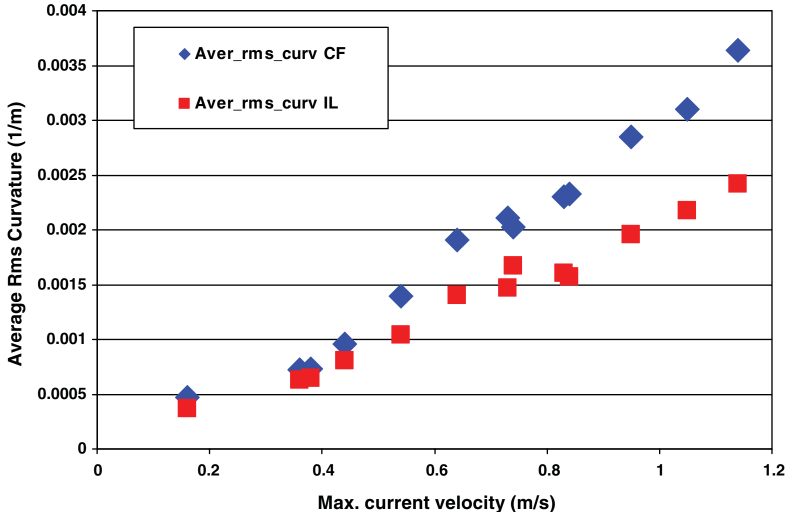

Fig. 14. Average curvature versus flow speed at top of riser.

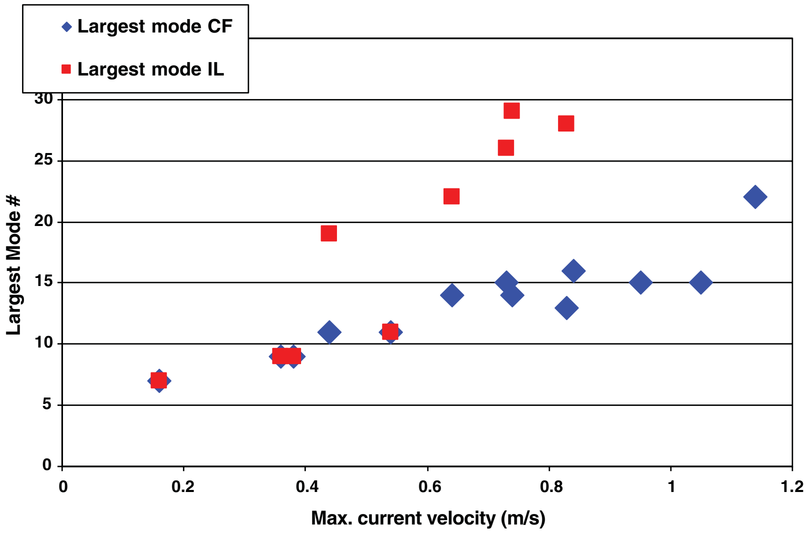

Fig. 15. Largest mode number with respect to displacement versus flow speed at top of riser.

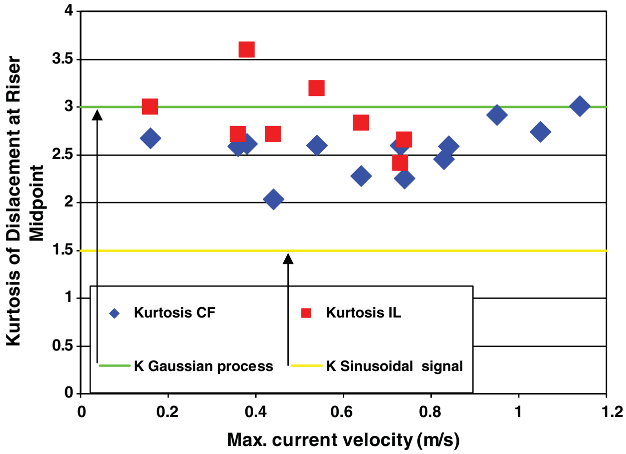

Fig. 16. Kurtosis versus flow speed at top of riser.

to be sinusoidal. For VIV a kurtosis value towards 1.5 may therefore indicate lock-in. Being in general more irregular than CF the IL response is expected to have higher kurtosis than CF. Fig. 16 shows kurtosis of the 13 analysed cases as a function of towing speed. For both CF and IL the kurtosis indicates a character of the response that is chiefly irregular. This is in agreement with the examples in Figs. 8 and 9. The kurtosis does not seem to be related to the towing speed in any obvious way. The lowest kurtosis value (for CF) is about 2, which happens for a tow speed of 0.44 m/s. It turns out that the CF response in this test had a strong unimodal character and a narrow response spectrum. It should be added that the kurtosis test for lock-in is not infallible. For example, if the oscillation has every character of lock-in, yet with a slowly varying amplitude, the kurtosis may be significantly greater than 1.5.

10. Conclusion

One objective of the Hanøytangen experiments was to provide data on high-mode riser VIV in a well-defined sheared current. Bending strain was measured in two orthogonal directions at 29 locations on the riser. A modal approach was used to identify modes of vibration, horizontal displacements and curvature. The method uses given mode-shapes and least-squares fitting of the model to the measurements. In order to get realistic estimates for the displacements, and hence the time-varying shape of the riser, noise filtering is essential. An error analysis was carried out that enabled checking the quality of the calculations. Due to spatial aliasing, modes above the 29th should not be identified, which was a significant problem for the IL analysis. Using nonequidistant sensor placement is a possible way of getting around this problem.

The experiments gave VIV responses that were rich in participating modes and frequency components. The average r.m.s. displacement for CF along the riser is independent of towing speed and about 1/4 diameter in magnitude. This is lower than reported from comparable experiments. The reason is not known. For IL, the average displacement is 0.05–0.08 diameters. Since the IL vibrations occur at higher frequency than CF, the IL curvatures are comparable to those of CF. This means that in fatigue considerations, IL response cannot be neglected. For low speeds the r.m.s. displacement is about uniform over the length of the riser, whereas a more triangular shape is seen at higher towing speeds. It is inferred that the riser response consisted mainly of travelling waves. No case of lock-in was seen. As a consequence of the nonuniform (triangular) current profile the VIV responses are highly irregular, i.e. broad-banded with respect to frequency content. The frequency of the highest spectral peak seems to vary linearly with the towing speed for both CF and IL, the IL peak frequency being about twice the CF peak frequency. The irregular character is confirmed by analysis of kurtosis. The degree of irregularity seems to increase with the flow speed.

Acknowledgements

The present work has been supported by the Norwegian Deepwater Program (NDP), the Norwegian Marine Technology Research Institute AS (MARINTEK) and the Centre of Ships and Ocean Structures (CeSOS) at the Norwegian University of Science and Technology (NTNU).

References

Baarholm, G.S., Larsen, C.M., Lie, H., 2006a. Reduction of VIV using suppression devices–an empirical approach. Marine Structures, accepted for publication.

Baarholm, G.S., Larsen, C.M., Lie, H., 2006b. On fatigue damage accumulation from in-line and cross-flow vortex-induced vibrations on risers. Journal of Fluids and Structures 22, 109–127.

Blevins, R.D., 1990. Flow-Induced Vibration, second ed. Van Nostrand Reinhold, New York.

Étienne, S., Biolley, F., Fontaine, E., Le Cunff, C., Heurtier, J.M., 2001. Numerical simulations of vortex-induced vibrations of slender flexible offshore structures. In: Proceedings of the the 11th International Offshore and Polar Engineering Conference, Stavanger, Norway, pp. 419–425.

Gopalkrishnan, R., 1993. Vortex-Induced Forces on Oscillating Bluff Cylinders. Ph.D. Thesis, MIT, Cambridge, MA, USA.

Herfjord, K., Larsen, C.M., Furnes, G., Holmås, T., Randa, K., 1999. FSI-simulations of vortex induced vibrations of offshore structures. In: Kvamsdal, et al. (Eds.), Proceedings of the Computational Methods for Fluid–Structure Interaction. Tapir, Trondheim, Norway, pp. 283–303.

Huse, E., Kleiven, G., Nielsen, F.G., 1998. Large scale model testing of deep sea risers. In: Proceedings of the Offshore Technology Conference, Houston, Texas, OTC 8701.

Huse, E., Kleiven, G., Nielsen, F.G., 1999. VIV-induced axial vibrations in deep sea risers. In: Proceedings of the Offshore Technology Conference, Houston, Texas, OTC 10932.

Kaasen, K.E., 2001. Optimizing sensor locations for identification of riser VIV modes. In: Proceedings of the 11th International Offshore and Polar Engineering Conference (ISOPE), Norway.

Kaasen, K.E., Lie, H., Solaas, F., Vandiver, J.K., 2000. Norwegian deepwater program: analysis of vortex-induced vibrations of marine risers based on full-scale measurements. In: Proceedings of the Offshore Technology Conference, Houston, Texas, OTC 11997.

Kleiven, G., 2002. Identifying VIV vibration modes by use of the empirical orthogonal functions technique. In: Proceedings of the 21st International Conference on Offshore Mechanics and Arctic Engineering, Oslo, Norway.

Larsen, C.M., Koushan, K., 2005. Empirical model for the analysis of vortex induced vibrations of free spanning pipelines. EURODYN Conference, Paris, France.

Lie, H., Larsen, C.M., Vandiver, J.K., 1997. Vortex induced vibrations of long marine risers; model test in a rotating rig. 16th International Conference on Offshore Mechanics and Arctic Engineering, Yokohama, Japan.

Lie, H., Mo, K., Vandiver, J.K., 1998. VIV model test of a bare and staggered buoyancy riser in a rotating rig, Paper OTC 8700, Offshore Technology Conference, Houston.

MARINTEK, 2001. VIVANA—Theory Manual. MARINTEK Report MTF00-023, MARINTEK, Trondheim, Norway.

MARINTEK, 2003. RIFLEX v. 3.2—Program Documentation. MARINTEK, Trondheim, Norway.

Moe, G., Arntsen, Ø.A., Hoen, C., 2001. VIV analysis of risers by complex modes. In: Proceedings from the International Symposium on Offshore and Polar Engineering, IL-38.

Sarpkaya, T., 1978. Fluid forces on oscillating cylinders. Journal of The Waterway, Port, Coastal and Ocean Division 104, 275–290.

Sheppard, D.M., Omar, A.F., 1992. Vortex-induced loading on offshore structures: A selective review of experimental work. Paper No. 6817. In: Proceedings of the 24th Offshore Technology Conference, Houston, USA.

Timoshenko, S., Young, D.H., Weaver, W., 1974. Vibration Problems in Engineering, fourth ed. Wiley, New York.

Triantafyllou, M.S, Triantafyllou, G.S., Tein, D., Ambrose, B.D., 1999. Pragmatic riser VIV analysis. In: Proceedings from the Offshore Technology Conference, OTC 10931, Houston, USA.

Trim, A.D., Braaten, H., Lie, H., Tognarelli, M.A., 2005. Experimental investigation of vortex-induced vibration of long marine risers. Journal of Fluids and Structures 21, 335–361.

Vandiver, J.K., 1993. Dimensionless parameters important to the prediction of vortex-induced vibration of long, flexible cylinders in ocean currents. Journal of Fluids and Structures 7, 423–455.

Vandiver, J.K., Lee, L., 2003. SHEAR7 V4.2f Program Theoretical Manual.

Vikestad, K., 1998. Multi-frequency response of a cylinder subjected to vortex shedding and support motions. Ph.D. Thesis. Department of Marine Structures, Norwegian University of Science and Technology, Trondheim, Norway.

Willden, R.H.J., Graham, J.M.R., 2001. Numerical prediction of VIV on long flexible circular cylinders. Journal of Fluids and Structures 15, 659–669.